International Journal of Heat and Mass Transfer 109 (2017) 1004–1013

Contents lists available at ScienceDirect

International Journal of Heat and Mass Transfer

journal homepage: www.elsevier.com/locate/ijhmt

Lattice Boltzmann simulation of condensation in the presence of noncondensable gas

Mingjie Li [a,c], Christian Huber [b,c], Yutong Mu [a], Wenquan Tao [a,*]

[a] Key Laboratory of Thermo-Fluid Science and Engineering, Ministry of Education, School of Energy & Power Engineering, Xi'an Jiaotong University, Xi'an 710049, China
[b] Department of Earth, Environmental and Planetary Sciences, Brown University, Providence, RI 02912, United States
[c] School of Earth and Atmospheric Sciences, Georgia Institute of Technology, Atlanta, GA 30332, United States

ARTICLE INFO

Article history:
Received 22 October 2016
Received in revised form 15 February 2017
Accepted 16 February 2017

Keywords:
Lattice Boltzmann
Condensation
Noncondensable gas
Waste heat recovery
Surface wettability

ABSTRACT

In this paper we use the multiphase multispecies Lattice Boltzmann method to investigate the influence of non-condensable gas on condensation. Condensation on a horizontal cold wall as well as that on a vertical wall with droplet movement is investigaged. The presence of non-condensable gas obviously reduces the condensation mass rate as well as the heat flux compared to condensation from pure vapor. The waiting time before nucleation is increased with non-condensable gas, and the wetting characteristics are also changed (the contact angles are increased), which further influences the heat transfer. Correlations of the relationship between droplet diameter and condensing time for different surface wettability, or contact angles, as well as different air mass fraction are obtained. As for condensation on a surface parallel to the gravitational force, it's demonstrated that the presence of non-condensable gas reduces the droplet departure diameter and increases the period between subsequent droplet formation and departure.

1. Introduction

Condensation is a process commonly used in several applications such as waste heat boiler and heat exchanger due to its great performance in transferring heat through phase change. In all applications, the phase change is not that of a pure substance because of the presence of noncondensable gases such as air mixing with the condensing vapor. Under certain circumstances where the vapor is the only condensable phase, the presence of noncondensable gases plays a negative effect on heat transfer, and seriously reduce its efficiency. Overall, vapor condensation is a complex process because it involves phase change, multiphase flow and multiple components or species.

Several studies have been designed to explore boiling through numerical simulations. Direct numerical simulation based on two-film theory is one of the most widely used method to deal with condensation in the presence of noncondensable gases [1–10]. The condensing liquid and the noncondensable gas are assumed as two layers of fluid, the vapor diffuses across the noncondensable gas layer and then condenses at the interface. This method can only deal with film condensation, and cannot deal with complex vapor-liquid flow. Another common set of approaches is based on front tracking methods for interfaces such as the volume of fluid (VOF), level-set and phase change methods [11–17]. The phase change is often parameterized with experimental correlations, while in some other cases it is solved by an energy and mass balance equation directly at the interface through source terms for the phase change [18–23]. In these methods, a bubble (or droplet) and an interface have to be set there initially because the nucleation process during condensation cannot be simulated.

In the present study, we take a different approach as we aim to solve for the nucleation and flow process together in a self-consistent way. The model we use is based on the Lattice Boltzmann method (LBM), which is a mesoscopic solver that can simulate two-phase flows with complex time evolving interfaces (deformation, coalescence, breakup, etc.). Among all the LBM multiphase methods, the pseudo-potential model (Shan-Chen model) can be easily used to calculate multiphase and multispecies problem. The pseudo-potential approach is convenient in that it is a diffuse interface approach, which implies that there is no need to track the interface between the different phases. A significant advantage of the model is that we can apply a real gas equation of state and add a phase change source term into the energy equation which simultaneously allows us to model the nucleation process. These characteristics motivated our choice for the Shan-Chen (SC) model with a double distribution

* Corresponding author.
E-mail address: wqtao@xjtu.edu.cn (W. Tao).

http://dx.doi.org/10.1016/j.ijheatmasstransfer.2017.02.046
0017-9310/

function to deal with this multiphase (gas-liquid) multispecies (air, water vapor) phase change problem.

In the SC model, a pseudo-potential function is used to represent molecular interactions. Fluids can spontaneously separate into two phases or two species with two different densities under these interactions (spinodal decomposition). The phase interface is characterized by the variation of the fluid density for each phase [24–30]. Hazi and Markus [31] used the SC model to investigate boiling, where the source term for the phase is derived directly from the entropy balance equation based on an equation of state for real gases. Building from Hazi's method, Cheng et al. [32,33] improved on the pseudo-potential function as well as the source term to calculate both boiling and condensation. Li et al. [34] also used the pseudo-potential model to simulate two phase flow during pool boiling, which allowed them to reproduce the boiling curve and the influence of surface wettability on boiling accurately. They, however, solved the temperature field with a traditional finite-difference scheme.

All the above literatures focus on single component model with phase change (water-vapor). Zhang et al. [35] used the multiphase multicomponent SC model to study the condensation of humid air on a rough surface, however it is assumed that condensation is isothermal and that the phase changes does not affect the temperature distribution. Chen et al. [36] recently developed a multicomponent multiphase reactive transport processes with SC model for phase change. However, in their model, the phase change between vapor and liquid is not compatible with the real gas equation of state, they rather propose a special treatment of nodes undergoing phase change, which complicates the algorithm significantly.

In summary, it remains rather challenging to simulate the multiphase multispecies phase change problem self-consistently. In the present study, we propose a model to circumvent this challenge. We use the LB method to simulate the condensation with noncondensable gas, which deals with multiphase, multispecies and phase change all together. The model allows us to study the effect of non-condensable gas (impurities) on condensation and heat transfer. Its effect on surface wettability is also investigated.

2. Model description

2.1. Multiphase multicomponent pseudo-potential LBM model

In the case of two components where only one component goes through phase change, a two-component multiphase LBM is required. The multicomponent multiphase SC model treats each component with a corresponding distribution function. Based on the assumption of a single relaxation time commonly referred to as the Bhatnagar–Gross–Krook (BGK) model, the evolution equation for each component is given by:

$$f_i^\sigma(\vec{x}+\vec{e}_i^\sigma\delta_t, t+\delta_t) - f_i^\sigma(\vec{x},t) = -\frac{1}{\tau^\sigma}\left(f_i^\sigma(\vec{x},t) - f_i^{\mathrm{eq},\sigma}(\vec{x},t)\right) \tag{1}$$

where f_i^σ is the density distribution function of the component σ at position $\vec{x}$ and time t, τ is the relaxation time. $\vec{e}_i$ is the discrete velocity along the ith lattice direction, and f_i^{eq} is the equilibrium distribution. For the D2Q9 scheme,

$$\vec{e}_i = \begin{cases} 0, & i=0 \\ (\cos[(i-1)\pi/2], \sin[(i-1)\pi/2]), & i=1,2,3,4 \\ \sqrt{2}(\cos[(i-5)\pi/2+\pi/4], \sin[(i-5)\pi/2+\pi/4]), & i=5,6,7,8 \end{cases} \tag{2}$$

and

$$f_i^{\mathrm{eq}}(\vec{x},t) = \omega_i\rho\left[1 + \frac{\vec{e}_i\cdot\vec{u}}{c_s^2} + \frac{(\vec{e}_i\cdot\vec{u})^2}{2c_s^4} - \frac{\vec{u}^2}{2c_s^2}\right] \tag{3}$$

where ω_i are the weight factors and are given by $\omega_0 = 4/9$, $\omega_{1-4} = 1/9$ and $\omega_{5-8} = 1/36$. The lattice sound speed c_s is defined as $c_s^2 = c^2/3$, and $c = \delta x/\delta t$ with δx and δt the lattice spacing and time spacing respectively (set to 1). The fluid density ρ and fluid velocity $\vec{u}$ are obtained from the statistical moments of the distributions

$$\rho^\sigma = \sum_i f_i^\sigma \tag{4}$$

$$\rho^\sigma\vec{u}^\sigma = \sum_i \vec{e}_i f_i^\sigma \tag{5}$$

Finally, the kinematic viscosity is given by $\upsilon^\sigma = c_s^2(\tau^\sigma - 0.5)\delta t$.

For a multicomponent system, there exists both intra- and inter-molecular interaction forces. The interaction potential ψ^σ is introduced in the SC model to include the interaction forces between particles. The intra-molecular interaction is generally defined as

$$\vec{F}_f^{\sigma\sigma}(\vec{x}) = -G^{\sigma\sigma}\psi^\sigma(\vec{x})\sum_i \omega(\vec{e}_i^2)\psi^\sigma(\vec{x}+\vec{e}_i)\vec{e}_i \tag{6}$$

where $\psi^\sigma(\vec{x})$ is the pseudo-potential function, G is a coefficient that sets the strength of the interaction and $\omega(\vec{e}_i^2)$ are weighting factors. The latter are set to $\omega(\vec{e}_i^2) = 1/3$ for the four nearest neighbors and 1/12 for the neighbors along the diagonal [37].

The interaction force between two components is shown as:

$$\vec{F}_f^{\sigma\bar{\sigma}}(\vec{x}) = -G^{\sigma\bar{\sigma}}\varphi^\sigma(\vec{x})\sum_i \omega(\vec{e}_i^2)\varphi^{\bar{\sigma}}(\vec{x}+\vec{e}_i)\vec{e}_i \tag{7}$$

where φ^σ and $\varphi^{\bar{\sigma}}$ are different from ψ^σ and $\psi^{\bar{\sigma}}$ [36]. For two components system φ^1 and φ^2 are designed to enforce the proper distribution of the two components at equilibrium. It was shown that $\varphi^1(\rho_2) = 1 - \exp(-\rho_2/\rho_{20})$ and $\varphi^2(\rho_1) = a_0 - \exp(-\rho_1/\rho_{10})$, providing a suitable set of functions [36]. The value of $G^{\sigma\bar{\sigma}}$, a_0, ρ_{10} and ρ_{20} are critical for the multicomponent multiphase system and also control the magnitude of the mutual diffusivity in the gas phase. After many test simulations, we set $G^{12} = G^{21} = 0.00001$, $a_0 = 0.9$, $\rho_{10} = 6$ and $\rho_{20} = 6$ which provide a set of parameters that recovers Laplace law accurately[36–39].

The interaction force between solid and fluid, which controls wetting, is given by:

$$\vec{F}_s^\sigma(\vec{x}) = -g_s^\sigma\psi^\sigma(\vec{x})\sum_i \omega(\vec{e}_\alpha^2)\psi(\rho_w)s(\vec{x}+\vec{e}_\alpha)\vec{e}_\alpha \tag{8}$$

where g_s^σ is a coefficient that sets the strength of the fluid–solid interaction for component σ, $s(\vec{x}+\vec{e}_\alpha)$ is the indicator function flagging the solid when its value is 1 and fluid when equals to 0.

In this paper, component 1 and 2 refer to the condensable and noncondensable gas, respectively. The noncondensable gas component is considered an ideal fluid, which requires G^{22} to be zero. The condensable component is treated as non-ideal fluid following the P-R EOS [34,40]:

$$p_{\mathrm{EOS}} = \frac{\rho Rt}{1-b\rho} - \frac{a\alpha(T)\rho^2}{1+2b\rho-b^2\rho^2} \tag{9}$$

where

$\alpha(T) = \left[1 + (0.37464 + 1.54226\omega - 0.26992\omega^2)\times(1-\sqrt{T/T_c})\right]^2$, $a = 3.0/49.0$, $b = 2.0/21.0$ and $R = 1.0$. The effective mass of condensable component is then $\psi^1(\vec{x}) = \sqrt{2(p_{\mathrm{EOS}} - \rho c_s^2)/gc_0^2}$ [40].

The velocity shift force scheme[24] is used here by replacing velocity in Eq. (5) with:

$$\vec{u}^{\sigma*} = \vec{u}' + \frac{\tau_\sigma}{\rho_\sigma}\vec{F}^\sigma \tag{10}$$

where $\vec{u}' = \left(\sum_\sigma \rho_\sigma \vec{u}^\sigma/\tau_\sigma\right)/(\sum_\sigma \rho_\sigma/\tau_\sigma)$ is the common velocity of all the components and $\vec{F}^\sigma$ is the body force acting on the σth component, which includes $\vec{F}_f^{\sigma\sigma}$, $\vec{F}_f^{\sigma\bar{\sigma}}$, $\vec{F}_s^\sigma$, and gravity.

Finally, the actual physical velocity is the average velocity before and after the collision and is given by

$$\vec{u}_r = \frac{\sum_\sigma \rho_\sigma \vec{u}^\sigma + \frac{\Delta t}{2}\sum_\sigma F_\sigma}{\sum_\sigma \rho_\sigma} \tag{11}$$

The pressure of the domain is calculated with [36]:

$$p = c_s^2 \sum_\sigma \rho_\sigma + \frac{1}{2}c_s^2 \sum_\sigma G^{\sigma\sigma}[\varphi^\sigma(\vec{x})]^2 + \frac{1}{2}c_s^2 \sum_{\bar{\sigma}\neq\sigma} G^{\sigma\bar{\sigma}}\varphi^\sigma(\vec{x})\varphi^{\bar{\sigma}}(\vec{x}) \tag{12}$$

2.2. Thermal phase change model

In this paper, we use a distinct distribution function to calculate temperature. The two components share the same temperature in the system. The entropy balance equation for the two components mixture (neglecting the viscous heat dissipation) is [41]:

$$\rho T Ds/Dt = \nabla\cdot(\lambda\nabla T) \tag{13}$$

where s is the entropy, λ is the thermal conductivity, and $Ds/Dt = \partial s/\partial t + \vec{u}\cdot\nabla s$.

Using the thermodynamic relation $Tds = c_v dT + T(\partial p_{\mathrm{EOS}}/\partial T)_\rho d(1/\rho)$ shown in [31], together with the continuity equation $D\rho/Dt + \rho\cdot\nabla\vec{u} = 0$, we can derive the temperature equation:

$$\frac{DT}{Dt} = \frac{1}{\rho c_v}\nabla\cdot(\lambda\nabla T) - \frac{T}{\rho c_v}\left(\frac{\partial p_{\mathrm{EOS}}}{\partial T}\right)_\rho \nabla\cdot\vec{u} \tag{14}$$

As $DT/Dt = \partial T/\partial t + \vec{u}\cdot\nabla T$, we get

$$\frac{\partial T}{\partial t} + \vec{u}\cdot\nabla T = \frac{1}{\rho c_v}\nabla\cdot(\lambda\nabla T) - \frac{T}{\rho c_v}\left(\frac{\partial p_{\mathrm{EOS}}}{\partial T}\right)_\rho \nabla\cdot\vec{u} \tag{15}$$

By adding $T\nabla\cdot\vec{u}$ on both sides of Eq. (15), and considering $\nabla\cdot(T\vec{u}) = \vec{u}\cdot\nabla T + T\nabla\cdot\vec{u}$ we can derive the following equation by further assuming a constant thermal inertia ρc_v in the domain [42]

$$\frac{\partial T}{\partial t} + \nabla\cdot(T\vec{u}) = \nabla\cdot\left(\frac{\lambda}{\rho c_v}\nabla T\right) - \frac{T}{\rho c_v}\left(\frac{\partial p_{\mathrm{EOS}}}{\partial T}\right)_\rho \nabla\cdot\vec{u} + T\nabla\cdot\vec{u} \tag{16}$$

We can use LBM to solve the first three terms of the temperature equation. $T\left[\nabla\cdot\vec{u} - \frac{1}{\rho c_v}\left(\frac{\partial p_{\mathrm{EOS}}}{\partial T}\right)_\rho \nabla\cdot\vec{u}\right]$ is treated as a phase change source term ϕ. p and $\vec{u}$ are both composite variables carried over from the two components SC solver. Equation (16) can be solved with LBM, with the source term added to the thermal distribution function

$$g_i(\vec{x}+\vec{e}_i\delta_t, t+\delta_t) - g_i(\vec{x},t) = -\frac{1}{\tau_T}(g_i(\vec{x},t) - g_i^{eq}(\vec{x},t)) + \delta_t\omega_i\phi \tag{17}$$

where g_i is the thermal distribution function, τ_T is the thermal relaxation time and g_i^{eq} is the equilibrium distribution. The thermal diffusivity is given by

$$\alpha = c_s^2(\tau_T - 0.5)\delta_t, \tag{18}$$

and the temperature is given by

$$T = \sum_i g_i. \tag{19}$$

3. Code validation

In this section we validate our code with two distinct tests: the isothermal two-phase two-component dynamics, and the non-isothermal phase change model during boiling.

3.1. Laplace law

The calibration with Laplace law is important for two-phase simulations, as it provides a test on the stress balance at the interface between the phases under static conditions. In this case, we embed a circular (2D) static bubble of component 2 in component 1 in a gravity-free field. The periodic computational domain consists of $200 * 200$ lattice nodes. The initial density for the liquid are 6.45 and 0.0045 outside and inside of the bubble, while they are set to 0.0015 and 0.09 for gas outside and inside the bubble. The temperature is set to $0.86T_c$ with T_c the critical temperature. As stated by Laplace law, the pressure jump across the phase interface Δp is linearly proportional to the reciprocal of the bubble radius $1/r$, and the slope of the relationship is the interfacial tension σ. It can be seen in Fig. 1 that Laplace law is reproduced satisfactorily.

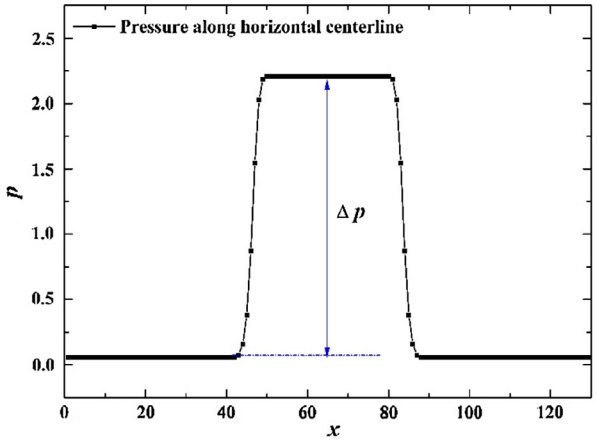

(a) Pressure along horizontal centerline

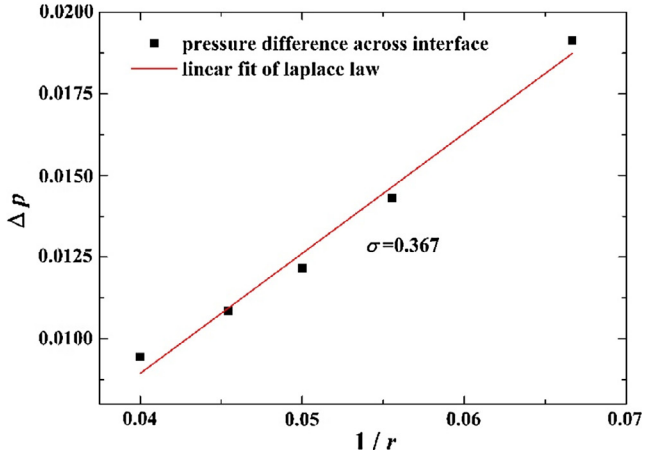

(b) Pressure difference vs bubble radius

Fig. 1. Calibration of Laplace law for a circular static bubble of component 2 in a liquid of component 1 in a gravity-free field.

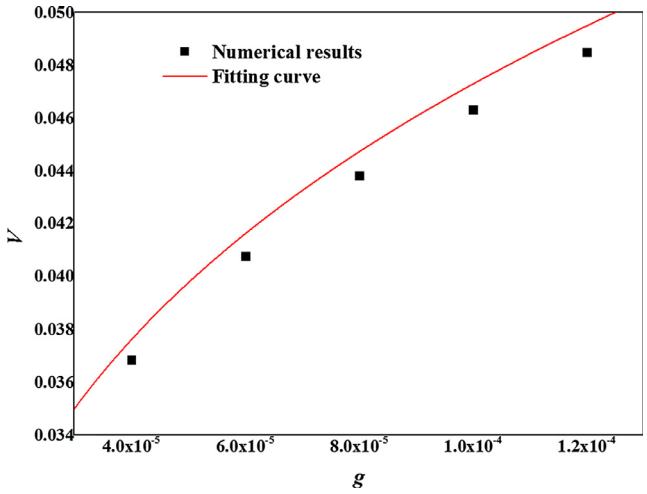

Fig. 2. Comparison of bubble rising velocities obtained by LBM and Eq. (20).

3.2. Dynamic validation

Then we valid this model by analysing the rising velocity of a bubble in saturated liquid under dynamic conditions. The velocity can be described as [43]:

$$V = 1.18\left[\frac{\sigma g(\rho_l - \rho_v)}{\rho_l^2}\right]^{0.25} \tag{20}$$

The relationship of velocity at various gravity is shown in Fig. 2. It can be seen that the it agrees quite well with Eq. (20), which demonstrates the dynamic validation of Shan-Chen model used in this paper.

3.3. Phase change and thermal model during boiling

We model nucleation boiling on a solid surface within a chamber cavity with the phase change model described above. The computational domain consists of $80 * 400$ lattice nodes with a solid wall at the bottom. The thickest part of the wall is 20 lattice units (or l.u.), the arc radius is 20 l.u., and the thinnest part of the solid is 10 l.u. Initially the domain is filled with a saturated liquid with a density of 6.5 at temperature $T = 0.86T_c$. The top boundary of the computational domain is set as an outflow, while left and right boundaries are periodic and the bottom is bounce-back condition with a constant higher temperature of $1.15T_c$. The nucleation process associated with boiling as well as the buoyant rise of bubbles are shown in Fig. 3. As the bottom of the chamber has a higher temperature than the rest of the domain, it is the location where boiling first takes place in the cavity. It can be seen in Fig. 3(a) that the density of the heated fluid first decreases, which is consistent with the equation of state. As time goes on, the lower density zone expands, and then develops into a bubble attached by capillary forces to the bottom of the domain, see Fig. 3(b) and (c). As more heat is transferred to the domain through the bottom boundary, the bubble grows, forms a bubble neck, and finally departs from the bottom wall, see Fig. 3(d), (e). The leftover vapor grows into another bubble as shown in Fig. 3(f)–(h). The detached bubble rises up while shrinking because of condensation, and finally disappears before reaching the upper boundary. This is because the detached bubble is not stable with the ambient liquid and its size is smaller than the critical bubble radius [31]. Given a greater buoyancy force and a greater thermal input at the boundary, the bubble will rise to the upper boundary.

Generally, the bubble departure diameter D_d and departure frequency f are two variables used to characterize the boiling process. The correlations of D_d and f reported by [44–46] are:

$$D_d = c_1\left(\frac{\sigma}{g(\rho_l - \rho_v)}\right)^{0.5} \tag{21}$$

$$f^{-1} = c_2 D_d\left(\frac{\sigma g(\rho_l - \rho_v)}{\rho_l^2}\right)^{-0.25} \tag{22}$$

where c_1 and c_2 are constant dimensionless coefficients. The numerical simulation results obtained for different gravity values are shown in Figs. 4 and 5 in lattice units. The exponent of the fitting curve to the model results for the departure diameter is −0.492, and −0.731 for bubble release period, which agree very well with the correlations reported above.

4. Condensation with noncondensble gas

In this section, we study condensation in the presence of noncondensable gas. First, we simulate condensation on a plate in the absence of gravity to investigate the effect of noncondensable gas on droplet generation and growth. Then, we simulate condensation on a vertical plate with gravity to study the effect of noncondensable gas on droplet departure radius and frequency.

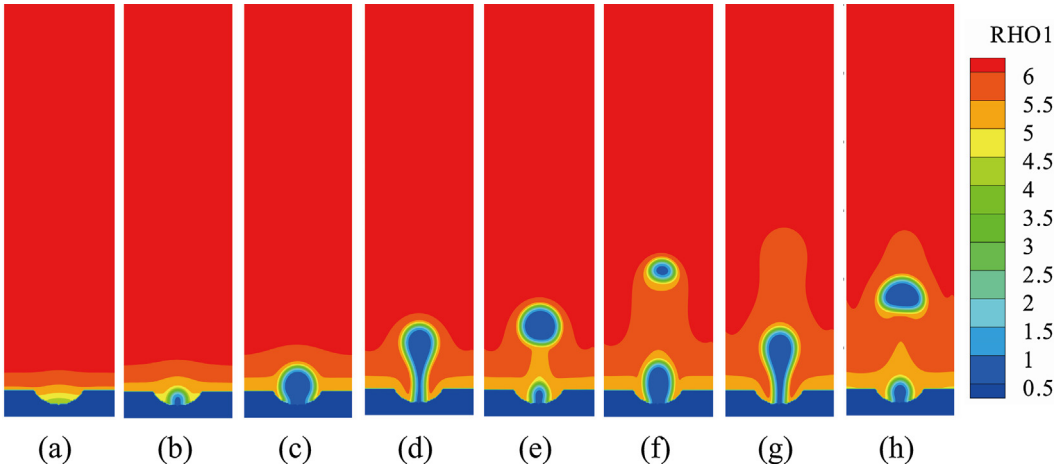

Fig. 3. Nucleation and bubble rise during boiling indicated by density contour.

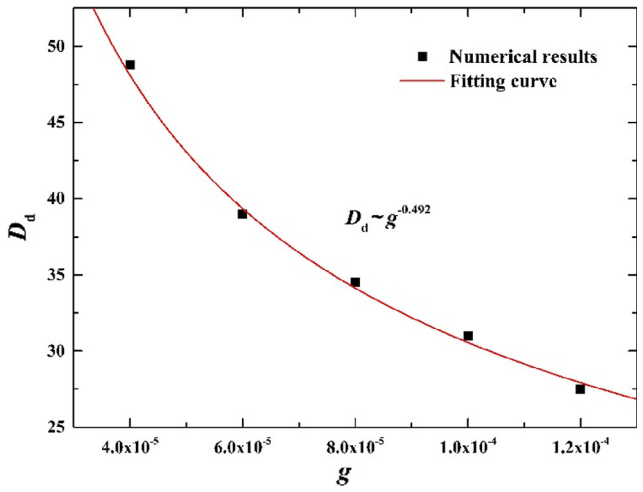

Fig. 4. Bubble departure diameter at various gravity values.

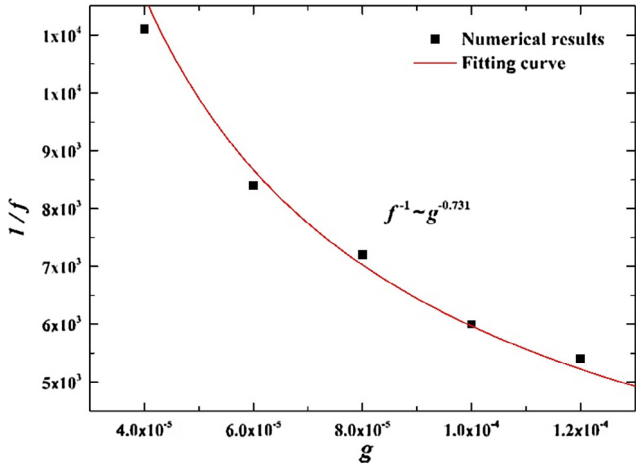

Fig. 5. Bubble departure period at different gravity values.

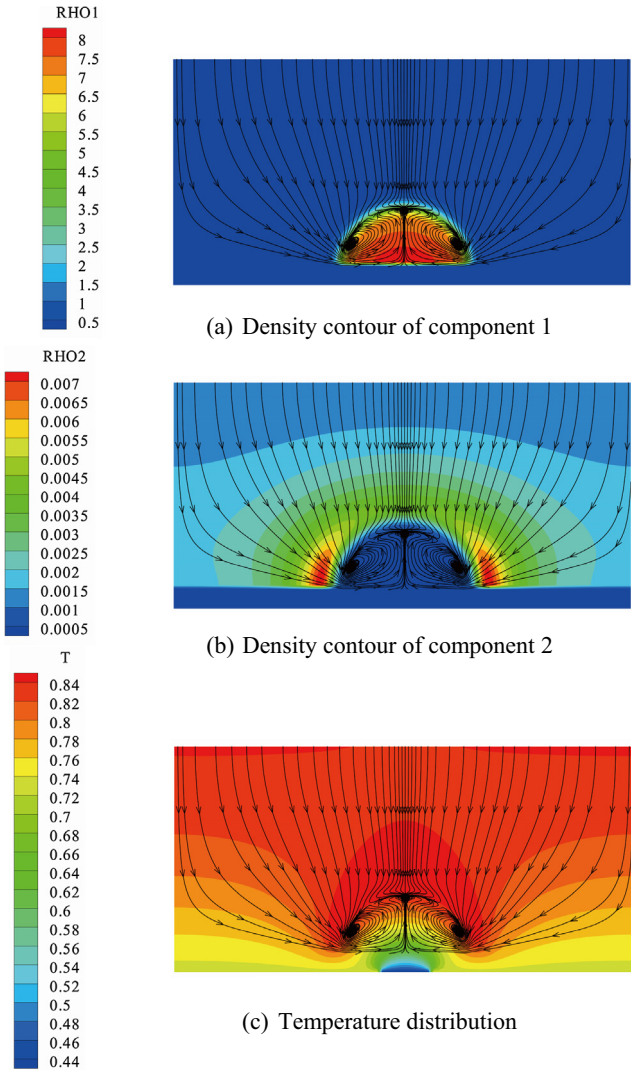

Fig. 6. Condensation with noncondensable gas on a colder wall.

4.1. Condensation on plate

A cold thick wall with a small colder spot is set at the bottom boundary. Zou-He pressure boundary conditions are applied at the top. The left and right boundaries are again periodic. Gravity is neglected in these calculations. Initially the domain temperature is set at the saturated temperature and higher than the bottom wall temperature. The cooling next to the bottom wall leads to an increase in density followed by condensation of the condensable component. The density contour for the two components, the temperature distribution as well as velocity streamlines are shown in Fig. 6. We observe that hot gas flows towards the cold bottom wall, and a droplet of component 1 is formed with two vortices generated inside the droplet. Component 2, first accumulates on top of the interface, then at the two corners of the droplet adjacent to the bottom wall. This is because the condensable vapor fraction decreases at the interface due to the phase change into liquid, which leads to an increase in noncondensable gas fraction. The wetting behavior of the liquid is such that the noncondensable gas starts to accumulate in the corners.

The profiles of the droplet at time step t = 10,000 are plotted in Fig. 7. The black line represents the case for pure vapor condensation, the red line stands for an air mass fraction of 0.33%, and the blue line for an air mass fraction of 1.64%. The value of g_s in Eq. (8) is identical for the two components and equals to −0.04, 0, 0.04 and 0.11, respectively. In panels (a) to (c) we observe clearly that a larger g_s value leads to a solid wall that is more hydrophobic and the contact angle of the droplet is larger. The presence of the noncondensable gas reduces the diameter of the droplet irrespective of the wettability of the wall.

Interestingly, we find that the contact angles are affected by the fraction of non-condensable gas, an effect that is more evident for larger g_s and larger air fraction. This can be explained by the dependence of the molecular interaction potential on the vapor density. In Fig. 7 panel (d), when g_s, by extension, the contact angle, are large enough, the droplet detaches from the wall due to the non-wetting behavior of the liquid-solid interface. This phenomenon is especially obvious when considering a larger fraction of noncondensable gas. The effect of noncondensable gas on droplet contact angle is shown in Fig. 8 at t = 10,000. The presence of a non-condensable component increases the effective contact angle for three g_s value.

An important aspect of condensation with noncondensable gas is the effect it has on the heat transfer between the wall and the domain. Here, we compare the heat flux at the colder spot of the bottom wall (the node where the condensate nucleates) for three different g_s values −0.04, 0 and 0.04, which lead to different surface wettabilities. The local heat flux of te bottom solid wall is defined by:

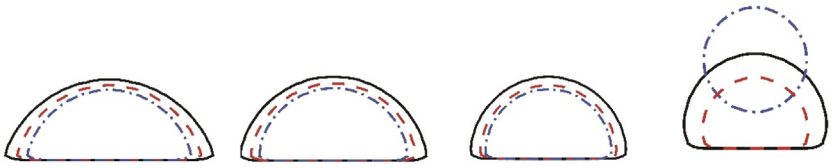

Fig. 7. Droplet profile for different air fraction at different value (The black line is for pure vapor condensation, the red line is for air mass fraction of 0.33%, and the blue line is for air mass fraction of 1.64%.) (For interpretation of the references to color in this figure legend, the reader is referred to the web version of this article.)

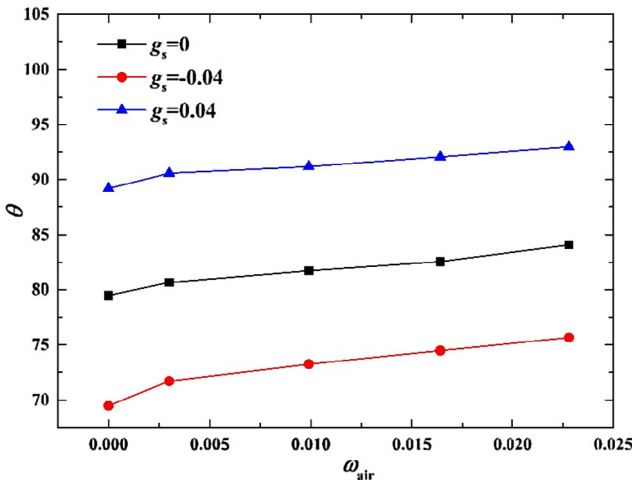

Fig. 8. Effect of noncondensable gas on contact angle.

$$q(x,t) = -\lambda \frac{\partial T}{\partial y}\Big|_{y=1} \tag{23}$$

and the results are shown in Fig. 9. The heat flux first decreases as the temperature difference between the wall and the surrounding gas decreases during cooling. Then nucleation occurs, and the heat flux increases rapidly. As the droplet grows the heat flux decreases because of the decrease in the temperature contrast between the cold wall and the liquid. For all three values of g_s or contact angles investigated in this paper, the calculated heat flux trends remain mostly identical before the onset of nucleation. This is because the total mass of the gas mixture is the same and pure vapor is the dominant component in the mixture, thus the heat transfer characteristic depends mostly on the vapor heat transfer behavior. In contrast, during nucleation, the heat flux with and without a non-condensable component are noticeably different. This is because during nucleation and early growth, the noncondensable gas acts as an obstacle through which vapor needs to diffuse in order for condensation to go on. Thus, the heat flux is seriously reduced by the presence of the non-condensable component. Interestingly, the mass fraction of noncondensable gas has a minor effect on the heat flux because all cases studied involved only a small amount of non-condensable gas. During the droplet growing period, the presence and amount of the noncondensable gas significantly reduces the heat flux compared to pure vapor. This is caused by the decrease in vapor mass fraction and relative increase in non-condensable gas fraction at the interface as condensation goes on. As a result, a thicker layer of noncondensable forms on top of the droplet, which increases the thermal resistance. Another reason for the decrease of heat flux can be seen from Fig. 7. For larger values of g_s, the contact angle is also greater and the contacting area between the droplet and the well is reduced which further decreases the heat transfer.

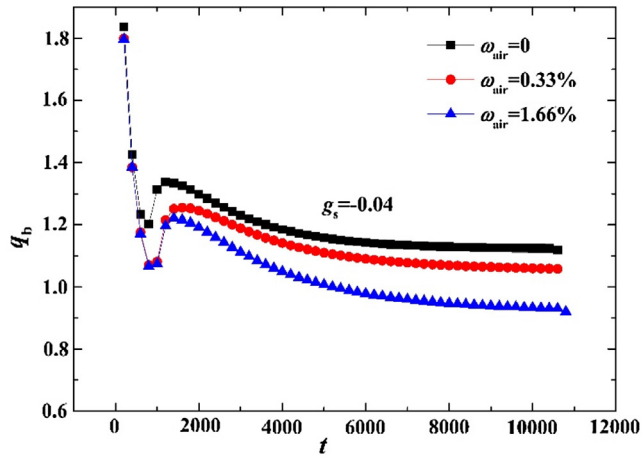

(a) local heat flux vs time at g_s =-0.04

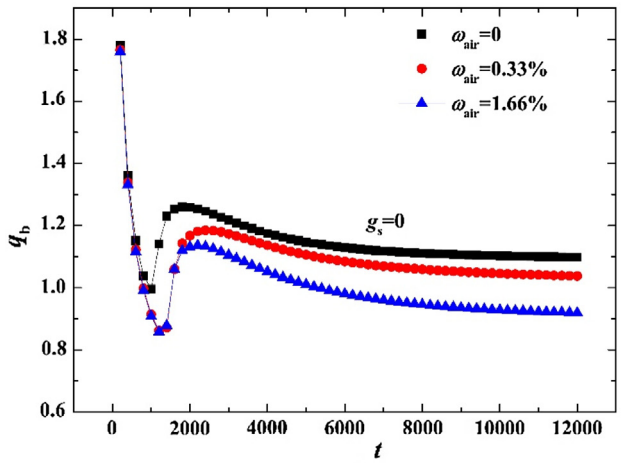

(b) local heat flux vs time at g_s =0

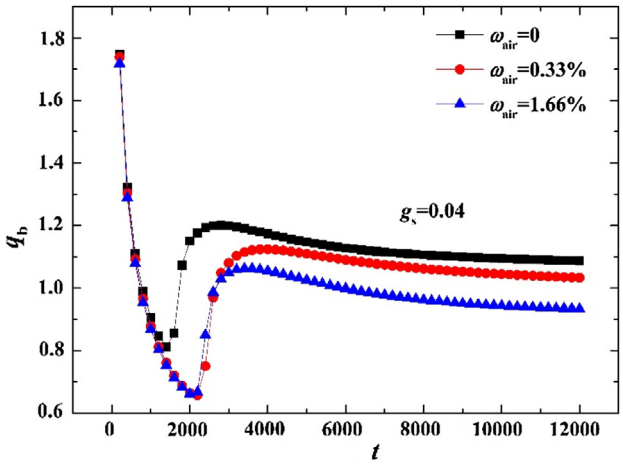

(c) local heat flux vs time at g_s =0.04

Fig. 9. Effect of noncondensable gas fraction on local heat flux.

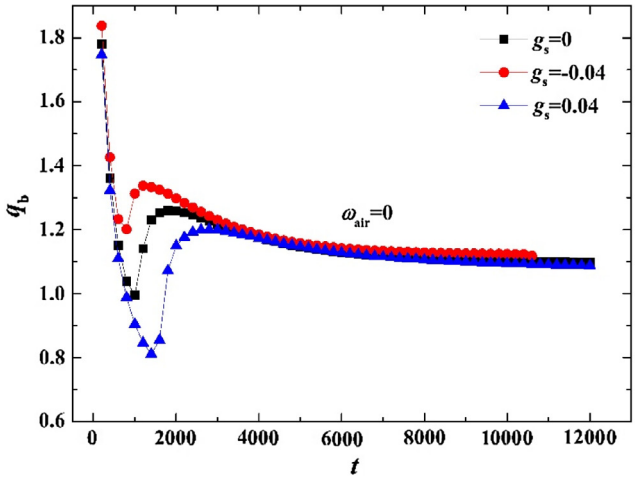

(a) local heat flux vs time at $\omega_{air} = 0$

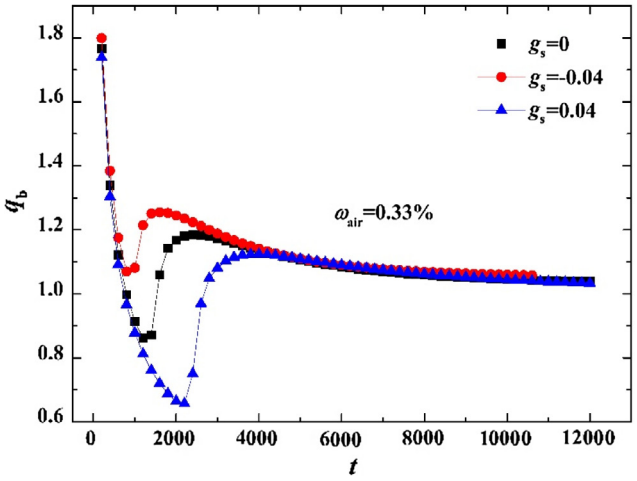

(b) local heat flux vs time at $\omega_{air} = 0.33\%$

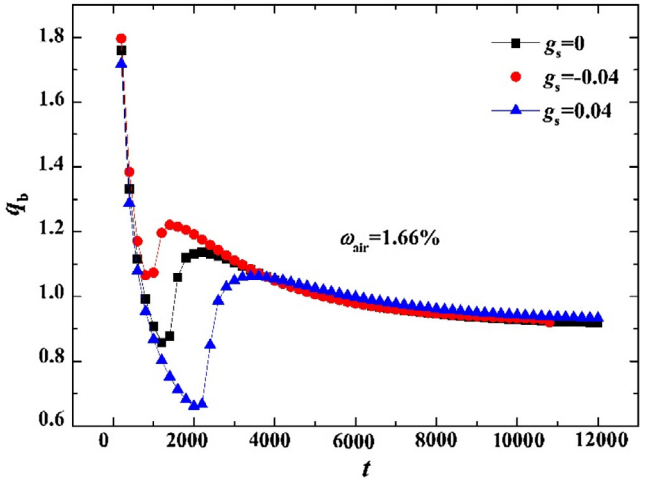

(c) local heat flux vs time at $\omega_{air} = 1.66\%$

Fig. 10. Effect of surface wettability on local heat flux.

Considering now the same mixture of air and vapor, we compare the heat flux for three different g_s values to find out the effect of surface wettability on condensation with and without a noncondensable gas. In Fig. 10 at a certain fraction of air, the final heat flux is the same in panels (a)–(c) for all the three surfaces with different wettability. However, the presence of noncondensable gas does

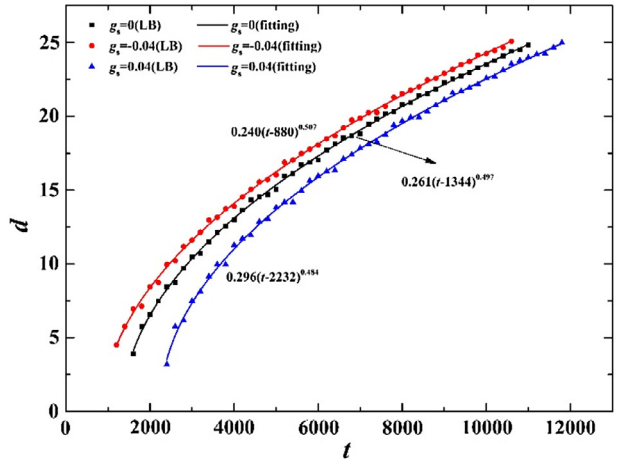

(a) Effect of noncondensable gas on droplet diameter

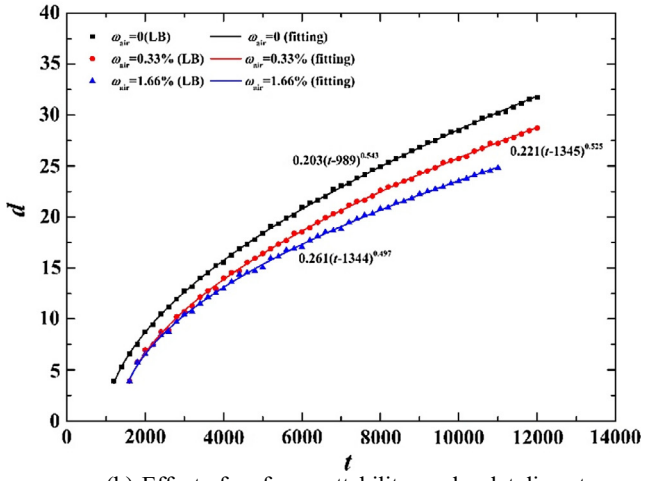

(b) Effect of surface wettability on droplet diameter

Fig. 11. Condensing droplet diameter variation along computational time at different air fraction and surface wettability.

have a significant effect on the condensation waiting time, as well as the nucleation time. Our results highlight that the hydrophobicity of the surface influences the waiting time, i.e. a greater contact angle yields a longer waiting time. The main reason for this phenomenon is that g_s controls the solid-fluid interaction and with a larger g_s value, more non-condensable gas is attracted onto the solid surface before nucleation. As pointed out above, the noncondensale gas plays the role of an obstacle, thus increasing the condensation time. This is also consistent with the understanding that condensation is enhanced on a hydrophilic rather than on a hydrophobic surface.

We also study the effect of non-condensable gas and surface wettability on the rate of droplet growth. The droplet diameter growth over time is plotted in Fig. 11 for pure vapor as well as two different air mass fractions for a given g_s value ($g_s = 0$). The bubble diameter increases with time, but the bubble growth rate decreases as condensation proceeds (panel a). As the bubble grows, the temperature difference decreases and so does the heat flux out of the domain through the bottom wall. Our simulations clearly show that the presence of non-condensable gas reduces the rate of droplet growth, i.e. the condensation rate. Fig. 11 panel (b) shows the growth rate of droplets for a given air mass fraction (1.66%) and various contact angles. It can be seen that the air mass fraction has more influence on the initial bubble growth rate, but that effect tails off as condensation proceeds.

Table 1
Fitting coefficients for droplet diameter in Eq. (24).

ω_{air}	$g_s = -0.04$		$g_s = 0$		$g_s = 0.04$	
	t_0	b	t_0	b	t_0	b
0	681	0.554	989	0.543	1577	0.522
0.33%	893	0.534	1345	0.525	2312	0.502
1.66%	880	0.507	1344	0.497	2232	0.484

The relationship between droplet diameter and condensing time for different g_s, or contact angles, as well as different air mass fraction can be fitted with

$$d = a * (t - t_0)^b \tag{24}$$

The fitting results are listed in Table 1. The exponent b and prefactor a control the condensing rate, while t_0 measures the waiting time before nucleation. Our results show that the power b

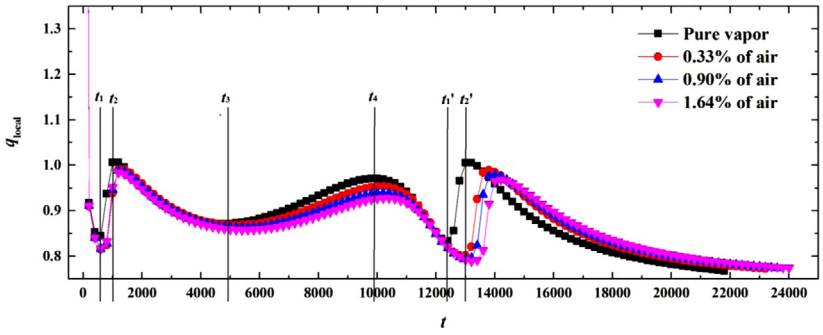

Fig. 12. Local heat flux of the colder spot.

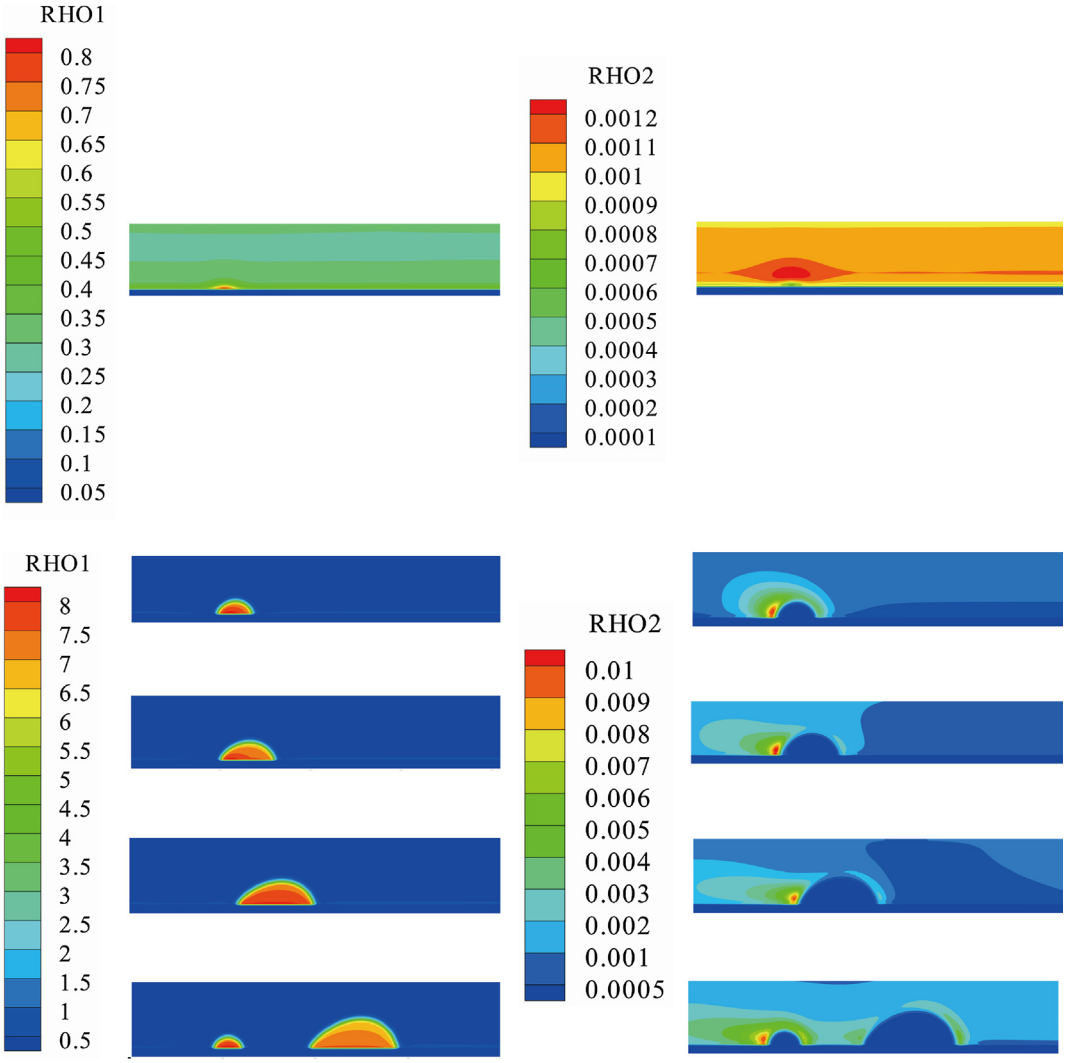

Fig. 13. Density contour for two components in the 5 periods (with gravity pointing to the right of the domain).

decreases and the waiting time t_0 increases with the presence of non-condensable gas, which is consistent with our discussion above (Fig. 9).

4.2. Condensation with gravity

In this section, we study condensation of vapor on a vertical cold wall and the subsequent motion of the droplet because of gravity (here pointing to the right of the domain). The bottom boundary shown in the paper is a solid wall with a temperature $0.5T_c$, and the small cold spot is $0.85T_c$. Left and right boundaries are periodic, and the top boundary is a pressure boundary imposed with the Zou-He condition. The value of g_s and gravity g are set to -0.05 and $1e^{-4}$, respectively. The local heat flux at the colder spot is plotted in Fig. 12. During the waiting time 0–t_1, before nucleation occurs, the heat flux decreases because of the cooling of the gas close to the bottom wall. Then the heat flux increases suddenly during t_1–t_2, where nucleation occurs and a droplet is formed. As the droplet grows during the interval t_2–t_3, the heat flux decreases again because of the temperature difference between the liquid and solid wall decreases. Then, during the interval t_3–t_4, the weight of the droplet becomes large enough for the gravity to overcome capillary stresses and the droplet starts to move away from the nucleation site and it is replaced by a hot mixture of vapor and air which leads to an increase of heat flux again. During the stage t_4–t_1', the wall is coated by the gas mixture and heat flux decreases as the mixture is cooled. Then a new condensation cycle begins, and a new droplet will be generated at the initial cold position.

The condensation process with non-condensable gas can be divided into the same 5 stages. It can be also seen from Fig. 12 that the presence of non-condensable gas delays the generation and departure time of the first droplet, as well as the generation of the second droplet. The delay is proportional to the mass fraction of non-condensable gas in the mixture. This phenomenon can be explained by the fact that the thermal resistance and the contact angle are greater compared to the case with a pure vapor gas which decreases the heat flux from the gas to the wall.

The density contours for the two components captured during each of the 5 periods are shown in Fig. 13. We observe that the advancing and receding contact angles are different due to gravity. As for the noncondensable gas, because the droplet impedes the buildup of noncondensable in the direction of gravity, it accumulates in the left corner of the droplet.

The presence of air mixed to vapor also influences the departure diameter of the droplet. In Fig. 14(a), we show that the condensing droplet has the largest departure diameter for pure vapor, while it decreases linearly with the mass fraction of air. The presence of non-condensable gas slightly increases the contact angle, as shown in Fig. 7, which reduces the contact area between the droplet and the wall and facilitates departure. As for the effect of gravity, the departure diameter is smaller for larger gravitational acceleration, which is consistent with a balance between gravitational and capillary forces on the droplet. As expected (see panel (b)), the condensing period for pure vapor is the shortest, and then increases linearly with air mass fraction.

The departure diameter of the droplet is also influenced by the wetting characteristics of the multiphase system. In Fig. 15, we show that for larger contact angles, the departure diameter is

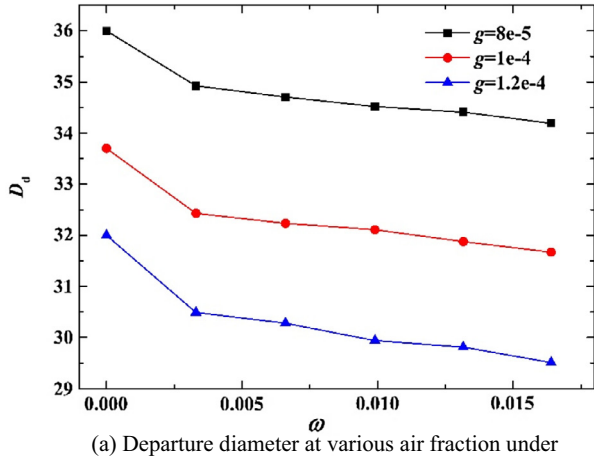

(a) Departure diameter at various air fraction under three different gravity values

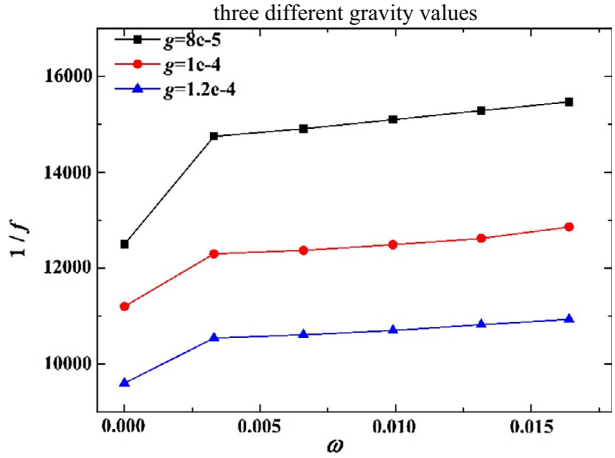

(b) Droplet generation period at various air fraction under three different gravity values

Fig. 14. Effect of air fraction at different gravitational acceleration.

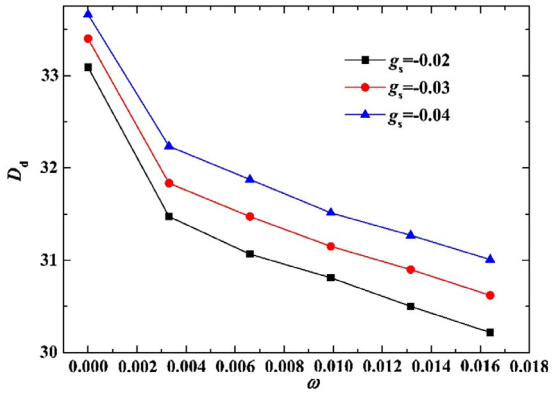

(a) Departure diameter at various air fraction under three different surface wettability values

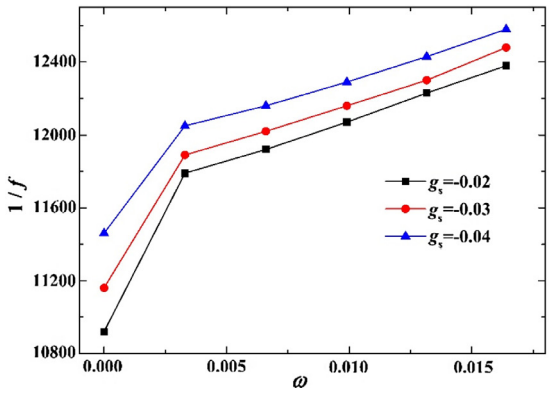

(b) Droplet generation period at various air fraction under three different surface wettability values

Fig. 15. Effect of air fraction for different surface wettability.

smaller. The departure period increases as the contact angle increases because condensation is inhibited on a hydrophobic surface.

5. Conclusion

In this paper we use the Lattice Boltzmann method to investigate the influence of non-condensable gas on condensation. We find that the presence of non-condensable gas reduces the condensation mass rate (droplet growth) as well as the heat flux compared to condensation from pure vapor. Increasing the mass fraction of non-condensable gas in the domain exacerbates these effects. As a result, the waiting time before nucleation is increased with non-condensable gas, and the wetting characteristics are altered (increases the contact angle between the wall and the droplet) which further influences the heat transfer between the cold wall and the surrounding gas mixture. When condensation is taking place on a surface parallel to the gravitational force, our simulations demonstrate that the presence of non-condensable gas reduces the droplet departure diameter and increases the period between subsequent droplet formation and departure.

Acknowledgements

Financial support of this work was provided by the National Basic Key Research Program of China (973 Program) (2013CB228304), and the National Nature Science Foundation of China (51136004).

References

[1] P.F. Peterson, V.E. Schrock, T. Kageyama, Diffusion layer theory for turbulent vapor condensation with noncondensable gases, J. Heat Transf. 115 (1993) 998–1003.
[2] P.F. Peterson, Theoretical basis for the Uchida correlation for condensation in reactor containments, Nucl. Eng. Des. 162 (1996) 301–306.
[3] S.Z. Kuhn, V.E. Schrock, P.F. Peterson, An investigation of condensation from steam-gas mixtures flowing downward inside a vertical tube, Nucl. Eng. Des. 177 (1997) 53–69.
[4] J.L. Munoz-Cobo, A. Escriva, L.E. Herranz, Mechanistic modeling of steam condensation onto finned tube heat exchangers in presence of noncondensable gases and aerosols, under cross-flow conditions: aerosol fouling and noncondensable gases effects on heat transfer, J. Enhanc. Heat Transf. 11 (2004) 75–85.
[5] D.F. Che, D.Y.D. Yao, Z.N. Zhuang, Heat and mass transfer characteristics of simulated high moisture flue gases, Heat Mass Transf. 41 (2005) 250–256.
[6] Juan Carlos de la Rosa, Jose L. Munoz-Cobo, Alberto Escriva, Non-iterative model for condensation heat transfer in presence of non-condensable gases inside passive containment cooling vertical tubes, Nucl. Eng. Des. 238 (2008) 143–155.
[7] K.Y. Lee, M.H. Kim, Experimental and empirical study of steam condensation heat transfer with a noncondensable gas in a small-diameter vertical tube, Nucl. Eng. Des. 238 (2008) 207–216.
[8] G.H. Tang, H.W. Hu, Z.N. Zhuang, W.Q. Tao, Film condensation heat transfer on a horizontal tube in presence of a noncondensable gas, Appl. Therm. Eng. 36 (2011) 412–425.
[9] H. Nabati, Investigation on numerical modeling of water vapour condensation from a flue gas with high CO_2 content, Energy 3 (2011) 181–189.
[10] J.D. Li, CFD simulation of water vapour condensation in the presence of non-condensable gas in vertical cylindrical condensers, Int. J. Heat Mass Transf. 57 (2013) 708–721.
[11] W.H. Lee, A pressure iteration scheme for two-phase flow modeling, Multiphase Transport Fund. React. Safety Appl. 1 (1980) 407–431.
[12] W. Lee, R. Lyczkowski, The basic character of five two-phase flow model equation sets, Int. J. Numer. Meth. Fluids 33 (2000) 1075–1098.
[13] R. Kouhikamali, B. Hassanpour, K. Javaherdeh, Numerical simulation of forced convective evaporation in thermal desalination units with vertical tubes, Desalinat. Water Treat. 51 (2013) 1503–1510.
[14] E. Da Riva, D. Del Col, Numerical simulation of laminar liquid film condensation in a horizontal circular minichannel, ASME J. Heat Transf. 134 (2012), 051019-1-8.
[15] X.T. Cui, X.G. Li, H. Sui, H. Li, Computational fluid dynamics simulations of direct contact heat and mass transfer of a multicomponent two-phase film flow in an inclined channel at sub-atmospheric pressure, Int. J. Heat Mass Transf. 55 (2012) 5808–5818.
[16] Z. Yang, X. Peng, P. Ye, Numerical and experimental investigation of two phase flow during boiling in a coiled tube, Int. J. Heat Mass Transf. 51 (2008) 1003–1016.
[17] J.H. Wei, L. M Pan, D.Q. Chen, H. Zhang, J.J. Xu, Y.P. Huang, Numerical simulation of bubble behaviors in subcooled flow boiling under swing motion, Nucl. Eng. Des. 241 (2011) 2898–2908.
[18] R. Kouhikamali, Numerical simulation and parametric study of forced convective condensation in cylindrical vertical channels in multiple effect desalination systems, Desalination 254 (2010) 49–57.
[19] D.L. Sun, J.L. Xu, L. Wang, Development of a vapor–liquid phase change model for volume-of-fluid method in FLUENT, Int. Commun. Heat Mass Transf. 39 (2012) 1101–1106.
[20] Y.W. Zhang, A. Faghri, Numerical simulation of condensation on a capillary grooved structure, Numer. Heat Transf. Part A – Appl. 39 (2001) 227–243.
[21] L. Wang, B. Sundén, Numerical Simulation of Two-Phase Fluid Flow and Heat Transfer With or Without Phase Change Using a Volume-of-Fluid Model, in: 2004 ASME International Mechanical Engineering Congress and Exposition, November 13–20, 2004, Anaheim, California USA, 2004.
[22] S.W. Welch, J. Wilson, A volume of fluid based method for fluid flows with phase change, J. Comput. Phys. 160 (2000) 662–682.
[23] C. Aghanajafi, K. Hesampour, Heat transfer analysis of a condensate flow by VOF method, J. Fusion Energy 25 (2006) 219–223.
[24] X.W. Shan, H.D. Chen, Lattice Boltzmann model for simulating flows with multiple phases and components, Phys. Rev. E 47 (1993) 1815–1819.
[25] X.W. Shan, H.D. Chen, Simulation of nonideal gases and liquid-gas phase transitions by the lattice Boltzmann equation, Phys. Rev. E 49 (1994) 2941.
[26] X.W. Shan, G. Doolen, Multicomponent lattice-Boltzmann model with interparticle interaction, J. Stat. Phys. 81 (1995) 379–393.
[27] J. Park, X. Li, Multi-phase micro-scale flow simulation in the electrodes of a PEM fuel cell by lattice Boltzmann method, J. Power Sources 178 (2008) 248–257.
[28] Q.J. Kang, D. Zhang, S. Chen, Displacement of a two-dimensional immiscible droplet in a channel, Phys. Fluids 14 (2002) 3203–3214.
[29] Q.J. Kang, D. Zhang, S. Chen, Displacement of a three-dimensional immiscible droplet in a duct, J. Fluid Mech. 545 (2005) 41–66.
[30] Y. Xuan, Z. Yao, Lattice Boltzmann model for nanofluids, Heat Mass Transf. 41 (2005) 199–205.
[31] G. Hazi, A. Markus, On the bubble departure diameter and release frequency based on numerical simulation results, Int. J. Heat Mass Transf. 52 (2009) 1472–1480.
[32] S. Gong, P. Cheng, A lattice Boltzmann method for simulation of liquid-vapor phase-change heat transfer, Int. J. Heat Mass Transf. 55 (2012) 4923–4927.
[33] X. Liu, P. Cheng, Lattice Boltzmann simulation of steady laminar film condensation on a vertical hydrophilic subcooled flat plate, Int. J. Heat Mass Transf. 62 (2013) 507–514.
[34] Q. Li, Q.J. Kang, M.M. Francois, Y.L. He, K.H. Luo, Lattice Boltzmann modeling of boiling heat transfer: the boiling curve and the effects of wettability, Int. J. Heat Mass Transf. 85 (2015) 787–796.
[35] Q.Y. Zhang, D.K. Sun, Y.F. Zhang, M.F. Zhu, Lattice Boltzmann modeling of droplet condensation on superhydrophobic nanoarrays, Langmuir 30 (2014) 12559–12569.
[36] L. Chen, Q.J. Kang, Q. Tang, B.A. Robinson, Y.L. He, W.Q. Tao, Pore-scale simulation of multicomponent multiphase reactive transport with dissolution and precipitation, Int. J. Heat Mass Transf. 85 (2015) 935–949.
[37] X.W. Shan, Analysis and reduction of the spurious current in a class of multiphase lattice Boltzmann models, Phys. Rev. E 73 (2006) 047701.
[38] M.L. Liu, Z. Yu, T.F. Wang, J.F. Wang, L.S. Fan, A modified pseudopotential for a lattice Boltzmann simulation of bubbly flow, Chem. Eng. Sci. 65 (2010) 5615–5623.
[39] Z. Yu, L.S. Fan, An improved multi-component lattice Boltzmann method for simulation of gas-liquid flows with high density ratio, in: AIChE Annual Meeting, 2007.
[40] P. Yuan, L. Schaefer, Equations of state in a lattice Boltzmann model, Phys. Fluids 18 (2006) 042101.
[41] D. Anderson, G.B. McFadden, A. Wheeler, Diffuse-interface methods in fluid mechanics, Annu. Rev. Fluid Mech. 30 (1998) 139–165.
[42] X. Liu, C. Ping, Lattice Boltzmann simulation for dropwise condensation of vapor along vertical hydrophobic flat plates, Int. J. Heat Mass Transf. 64 (2013) 1041–1052.
[43] S. Gong, P. Cheng, Lattice Boltzmann simulation of periodic bubble nucleation, growth and departure from a heated surface in pool boiling, Int. J. Heat Mass Transf. 64 (2013) 122–132.
[44] W. Fritz, Berechnung des maximalvolume von dampfblasen, Phys. Z. 36 (1935) 379–388.
[45] N. Zuber, Nucleate boiling. The region of isolated bubbles and the similarity with natural convection, Int. J. Heat Mass Transf. 6 (1963) 53–78.
[46] H.T. Phan, N. Caney, P. Marty, S. Colasson, J. Gavillet, A model to predict the effect of contact angle on the bubble departure diameter during heterogeneous boiling, Int. Commun. Heat Mass Transf. 37 (2010) 964–969.